PAPER

Cascade reaction engineering on zirconia-supported mesoporous MFI zeolites with tunable Lewis–Brønsted acid sites: a case of the one-pot conversion of furfural to γ-valerolactone†

Kyung Duk Kim,[a] Jaeheon Kim,[a] Wey Yang Teoh, [iD][b] Jeong-Chul Kim,[a] Jun Huang [iD][c] and Ryong Ryoo [iD] *[ad]

Catalytic cascade reactions are strongly desired as a potential means of combining multistep reactions into a single catalytic reactor. Appropriate catalysts composed of multi-reactive sites to catalyze cascade reactions in a sequential fashion are central to such efforts. Here, we demonstrate a bifunctional zeolite catalyst with close proximity of Brønsted and Lewis acid sites through the synthesis of a mesoporous $ZrO_2[Al]MFI$ nanosponge (NS). The unique mesopores of the MFI-NS allow the confinement of zirconium oxide clusters (Lewis acid sites, LA) within the few-unit-cell-thin MFI aluminosilicate zeolite wall (Brønsted acid sites, BA). Such a structure is clearly distinct from the conventional MFI zeolite, where the agglomeration of zirconium oxide clusters onto the external surface area within the crystal bulk is not possible, resulting in segregated BA and LA sites on the internal and external zeolite, respectively. By bringing the BA and LA within $ZrO_2[Al]MFI$-NS 30, we uncovered a more efficient catalytic route for the conversion of furfural (100% within 2 h) to γ-valerolactone (GVL) (83%). This route is only evident when the long molecular diffusion path, in the most extreme case of physically mixed ZrO_2-(LA) and Al-zeolites (BA) (45% of GVL yield), is eliminated. Unlike the bifunctional ZrO_2–Al-beta (GVL yield of 75%), where the BA concentration is greatly compromised at the expense of LA formation, we also show that the $ZrO_2[Al]MFI$-NS is able to maintain a high density and good stability of both types of acids.

1. Introduction

The exploitation of efficient catalytic processes capable of converting renewable cellulosic biomass, especially lignocellulose, to versatile platform chemicals is of importance for the production of sustainable chemicals and fuels, conventionally obtained from crude oil.[1] Biomass-derived γ-valerolactone (GVL) has been identified as a versatile platform molecule due to its attractive physicochemical properties (low toxicity and biodegradability) and unique features that allow it to be transformed into a wide collection of bio-products, ranging from green fuels to bio-polymers.[2–4] Conventionally, the production of GVL from furfural is accomplished through multistep processing, where the combination of Brønsted and Lewis acidic

catalysts initially converts furfural into levulinic acid, followed by the reductive hydrogenation of levulinic acid to GVL over precious-metal catalysts such as Pt and Ru.[5] In spite of the burgeoning interest, the requirements of high-pressure hydrogen and the costly noble-metal catalysts required during the reductive hydrogenation step have been shown to impact the economic feasibility of this process negatively.[6,7] Hence, the catalytic transfer hydrogenation (CTH) route using the Meerwein–Ponndorf–Verley (MPV) reaction is often used as an alternative to reductive hydrogenation, in which the Lewis acids can serve as an efficient catalyst with the aid of secondary alcohols (*e.g.* 2-propanol, 2-butanol, and cyclohexanol) as an H-donor.

Zeolites containing isomorphously substituted-heteroatoms such as Sn and Zr, are often used as a catalyst for the CTH reaction due to the high intrinsic Lewis acid (LA) activity of single-atomic Sn or Zr sites.[8,9] Most conventionally, these heteroatom-containing zeolites can be obtained by a hydrothermal synthesis route. However, there remain a number of fundamental restrictions though these have been gradually overcome in recent years. For example, it is well-known that this route requires a long synthesis time (nearly one month) due to the extremely slow rate of heteroatom incorporation[8,10] and

[a]Center for Nanomaterials and Chemical Reactions, Institute for Basic Science (IBS), Daejeon 34141, Korea. E-mail: rryoo@kaist.ac.kr

[b]School of Chemical Engineering, The University of New South Wales, Sydney, NSW 2052, Australia

[c]Laboratory for Catalysis Engineering, School of Chemical and Biomolecular Engineering, Sydney Nano Institute, The University of Sydney, NSW 2006, Australia

[d]Department of Chemistry, KAIST, Daejeon, 34141, Republic of Korea

† Electronic supplementary information (ESI) available. See DOI: 10.1039/d0ra06915a

necessitates the use of a toxic chemical, *e.g.*, fluoride as mineralizing agent to incorporated heteroatoms effectively in the framework position.[8] These problems can be partially overcome through the advancement of a seeding-mediated synthesis route, nevertheless, this approach is often far from optimum. To circumvent these limitations, Sn- or Zr-containing zeolites were often obtained by a post-synthetic route consisting of demetallation and a subsequent remetallation step.[11,12] In this route, aluminosilicate or borosilicate zeolites initially synthesized and then treated with an acid solution to remove the framework Al- or B-species. A subsequent incorporation step is conducted on the defect sites of the framework to generate isolated tetrahedral single Sn or Zr sites. In this way, a several Lewis acid zeolites have been reported to exhibit excellent catalytic activity for the CTH reaction.[12–14] In addition, bifunctional zeolites could be prepared by adjusting the degrees of Al removal (BA sites) and heteroatom incorporation (LA sites).[11,12,15–17] Controlled densities of BA and LA sites within close proximity in bifunctional zeolites are spatially segregated such that they are aligned with the residence time of each reaction step, hence increasing GVL productivity.[11,12,15–18] Nevertheless, this process of controlled partial dealumination to obtain the optimum Si/Al ratio is highly sensitive, rendering the tuning of the BA–LA ratio in the product catalyst rather cumbersome with demetallation possibly leading to certain problems associated with the crystallinity of zeolites.

Another notable way to design a bifunctional BA–LA catalyst is to impregnate LA-components into aluminosilicate zeolites. It is well-known that some metal oxides such as ZrO_2, SnO_2, and TiO_2, can function as solid LA-catalysts when they form a nanoparticle-like morphology.[19–21] Therefore, it is simple to propose that if the tiny nanoparticles of metal oxides are supported inside the zeolite micropore channels, the resulting catalysts could exhibit high activity as a bifunctional BA–LA catalyst for the furfural to GVL. Unfortunately, the deposition of ZrO_2 nanoparticles onto the zeolite can in principle fulfill the requirements of LA sites; however, this has remained limited to the external surface of the zeolites as stability is not straightforward in the microporous channels of zeolites. The microporous exclusion of metal oxide nanoparticles is a common feature in which the high surface energy from small nanoparticles confers a large amount of mobility to migrate to external surfaces of the crystal zeolite.[22–24] Because microporous zeolites have a very low external surface area, small nanoparticles are more susceptible to agglomeration, inevitably limiting flexibility during the engineering of in-pore reactions. To circumvent the difficulty of ZrO_2 deposition within the narrow and tortuous zeolite micropores, here we employ the use of mesoporous MFI nanosponge (NS) consisting of MFI zeolite with mesoporous channels.[22,23,25,26] Silt-shaped mesoporous channels, bound by a few unit cells-thin MFI aluminosilicate zeolitic walls (BA-rich sites) with highly uniform diameters can strictly support ZrO_2 nanoparticles with the confinement contact effect of meso-micro pore walls, resulting in a high dispersion of ZrO_2 clusters (LA-rich sites) and thereby allowing very close proximity of BA–LA sites within cascade reaction distances. In addition, mesoporous MFI-NS have is reportedly

capable of rapid molecular diffusion under various catalytic reaction conditions.[22–24,27,28]

In this work, we demonstrate this concept *via* the one-pot conversion of furfural to GVL. BA–LA tunable $ZrO_2[Al]MFI-NS$ zeolites, whilst mitigating the various limitations of conventional zeolites, exhibit the efficient one-pot conversion of furfural with a high GVL yield (83%) without the need for hydrogen pressure and precious metals. In fact, the high stability of the $ZrO_2[Al]MFI-NS$ is further demonstrated through a number of recycling reactions with a minimal decrease in the performance outcome.

2. Experimental

2.1 Catalyst preparation

Detailed processes for the synthesis of pristine catalysts such as mesoporous MFI-NS, bulk-MFI, and the Beta catalysts used here are provided in the ESI.† ZrO_2-containing MFI zeolites were synthesized *via* impregnation as reported in previous work.[29] To prepare all of the zeolites (ZrO_2-[Al]MFI-NS, ZrO_2 bulk-MFI and ZrO_2-Al-beta), 0.032 mg of zirconium(IV) oxynitrate hydrate was dissolved into 5 ml of deionized water. 0.2 mg of zeolite was added to the aqueous solution. The mixture was stirred at 80 °C for 2 h until the excess water was removed. Subsequently, the zeolite powder dried at 80 °C for 6 h in an oven and calcined at 550 °C for 6 h.

2.2 Characterization of materials

Powder X-ray diffraction (XRD) patterns of zeolite materials were collected at two angles between 5° and 70° using a Rigaku Multiflex diffractometer equipped with Cu-Ka radiation ($\lambda = 0.1541$ nm) at 40 kV and 30 mA. Argon adsorption–desorption isotherms were obtained using an ASAP 2020 at 87 K. Prior to the adsorption measurements, all samples were degassed at 573 K for 6 h. The pore-size distributions were derived from the adsorption branch of the argon isotherms using non-linear density functional theory (NLDFT), with the assumption of cylindrical pores. The specific surface area was calculated from the adsorption branch in the P/P_0 range of 0.05–0.2 using Brunauer–Emmett–Teller (BET) equations. High-resolution scanning electron microscopy (SEM) images were taken with a FEI VERIOS 460 instrument operating at 1 kV in beam-deceleration mode. Transmission electron microscopy (TEM) images were obtained with a Tecnai microscope operating at 300 kV (G2F30). Before these measurements, the power sample was suspended in acetone by ultra-sonication. A few droplets of the suspended solution were placed on a Cu microgrid and dried under ambient conditions. The silicon, aluminum and zirconia loadings of the zeolite materials were determined by a Thermo IRIS Intrepid II XSP atomic emission spectrometer (ICP-AES). The solid ^{27}Al MAS NMR spectra were recorded using a Bruker Avance III 400WB spectrometer at room temperature operated at a B_0 field of 9.4 T with Larmor frequencies of 104.3 MHz. A sample spinning rate of 10 kHz using 4 mm rotors was used in all of the experiments.

The concentrations of the acid sites were measured using Fourier transform infrared (FT-IR) after adsorbing pyridine as

a probe molecule. Pyridine (Py) with a kinetic diameter of about 0.5 nm was used to detect the total number of Brønsted and Lewis acid sites existing on the internal pore walls and external surfaces of the zeolite crystals. 2,6-di-*tert*-butyl-pyridine (DTBP) was used to measure the Brønsted acid sites located on the external surfaces of the samples due to its larger kinetic diameter (0.8 nm) than the 10-ring channels (5.1 × 5.5 Å, 5.3 × 5.5 Å) of MFI zeolites. FT-IR spectra were acquired using a JASCO FTIR-6100, following a method reported in the literature.[30] Prior to the measurement, a self-supported zeolite wafer (*ca.* 10 mg cm^{-2}) was placed in a lab-made IR cell and evacuated at 400 °C for 4 h. Then, adsorption of the probe molecules (Py and DTBP) was carried out at 150 °C for 30 min at an equilibrium probe vapor pressure for 30 min. Desorption proceeded at the same temperature for 1 h, followed by the collection of the spectra at room temperature. All IR data were recorded with a resolution of 2 cm^{-1} by collecting 40 scans for a single measurement. For quantification of the total Brønsted and Lewis acid sites, the molar extinction coefficient [$\varepsilon(B)$ = 1.67 cm μmol^{-1} and $\varepsilon(L)$ = 2.22 cm μmol^{-1}] of the pyridine IR band at 1545 cm^{-1} and at ν = 1454 cm^{-1} was used. To calculate the concentration of external Brønsted acid sites, extinction coefficients for pyridine at ν = 1616 cm^{-1} were also used.

2.3 Catalytic reaction

The catalytic conversion of furfural was performed both in a thick-walled glass reactor and in 150 ml stainless reactor continuing a magnetic stir bar with thermal couple monitoring. Typically, prior to the reaction, all zeolites were activated under a dry nitrogen flow (30 ml min^{-1}) at 400 °C for two hours. After cooling the catalysts under a flow of N$_2$, the zeolite was transferred into the reactor. Subsequently, 0.04 M furfural at a 1 : 50 molar ratio of furfural to a 2-propanol solution (2-propanol as the solvent and hydrogen donor) was added to the rector. The mass ratio of the catalyst to furfural was 1 : 2.5. The reactor was heated to 170 °C in a temperature-controlled oil bath on a magnetic stir plate, and the product mixtures were collected at various times. The products were separated by filtration and analyzed by a gas chromatograph (youngling) equipped with a capillary column (Rtx-5 column, 30 m × 0.25 mm × 3 μm) and a flame ionization detector (FID). The products were identified from known standards and by gas chromatography-mass spectrometry (Agilent, Rtx-5 column, 30 m × 0.25 mm × 3 μm). The products were quantified based on the retention times and response factors of the internal standard chemicals (*n*-decane). In the catalyst recycling experiments (fourth cycles), the catalyst was separated from the reaction mixture using a centrifuge and washed with 2-propanol three times to remove any residuals and organics, followed by drying at 100 °C in an oven overnight. The cascade furfural conversion experiments were then carried out using the recovered catalyst with the same procedure described above.

2.4 Kinetic modeling

Kinetics modelling was carried out by fitting the time–concentration of the furfural reactant, GVL product and other intermediates, as described by the following set of ordinary different equations that describe the first-order reaction kinetics of each step in the cascade reactions:

$$\frac{d[\text{FAL}]}{dt} = -(k_3 + k_1)[\text{FAL}] + k_2[\text{FDA}] \tag{1}$$

$$\frac{d[\text{FDA}]}{dt} = k_1[\text{FAL}] - k_2[\text{FDA}] \tag{2}$$

$$\frac{d[\text{FA}]}{dt} = k_3[\text{FAL}] - (k_4 + k_5)[\text{FA}] \tag{3}$$

$$\frac{d[\text{AL}]}{dt} = k_4[\text{FA}] - k_6[\text{AL}] \tag{4}$$

$$\frac{d[\text{IPL}]}{dt} = k_5[\text{FA}] + k_6[\text{AL}] - k_7[\text{IPL}] \tag{5}$$

$$\frac{d[\text{GVL}]}{dt} = k_7[\text{IPL}] \tag{6}$$

where FAL, FDA, FA, AL, IPL and GVL are the abbreviations for furfural, furfural diisopropyl acetal, furfural alcohol, β-angelica lactone, isopropyl levulinate, and γ-valerolactone, respectively. Matlab code was used to perform the numerical integration and optimization. The global error, taken as the square of the difference between the estimated and observed values, was minimized to determine the best fit reaction rate constants. The global error is typically less than 3 × 10^{-5}.

3. Results and discussion

3.1 Physiochemical properties of the investigated catalysts

In the present work, two different types of zeolites were synthesized and compared to each other as a catalyst for the efficient one-pot conversion of furfural to GVL. The first sample was an MFI zeolite exhibiting the morphology of a nanosponge (NS) which was synthesized using dual structure-directing multiammonium surfactants.[25,26] As shown in Fig. S1,† the MFI zeolite-like nanosponge samples showed the presence of ultra-thin nanocrystals (2.5 nm), as corroborated by the broadened MFI peaks measured using XRD, corresponding to a single-unit-cell size along the (010) direction with irregular interconnection. The zeolite nanosheets were rigidly self-supported in a highly mesoporous structure. The adsorption–desorption isotherm is the characteristic type IV, exhibiting a rapid increase in the low-pressure region of P/P_0 < 0.1 and a mid-pressure jump with hysteresis from P/P_0 0.4 to 0.7 of relative pressure (Fig. S1†). The former is involved in micropore filling in the zeolite framework, while the later reflects the capillary condensation of gas in the intercrystalline mesopores between zeolite nanosheets, which is a distinguishing feature of disordered mesoporous materials.[31] [Al]MFI-NS samples with different Si/Al ratios *e.g.* 30, 60, and 100, used to investigate the effect of the density of the Brønsted acidity on the furfural conversion to GVL, were synthesized. These nanosponge samples are denoted as '[Al]MFI-NS *n* (*n* is the number denoting the Si/Al ratio)'. Another sample was MFI zeolite with a bulk crystalline morphology synthesized by a conventional method

using tetrapropylammonium hydroxide as a SDA.[22] The MFI framework structure was confirmed by XRD and the diameters of the particles ranged from 500 nm to 1 um according to STEM (Fig. S3†), which are denoted as 'bulk-MFI 30 (where the number denotes the Si/Al ratio)'.

In an ideal BA–LA zeolite catalyst, the availability of LA-rich sites (*i.e.*, through the deposition of LA-mediated metals, in our study, ZrO_2) should lie within the molecular distances of the active BA sites (*i.e.*, the MFI zeolite framework) in such a way that intermediates are exposed to the appropriate active sites, as required at every step of cascade reactions. In order to provide LA-rich sites on the zeolites, 5 wt% zirconium oxide (ZrO_2) was deposited onto [Al]MFI-NS samples with different ratios of Si/Al, denoted as 'ZrO_2-[Al]MFI-NS *n*'. For comparison, bulk-MFI 30 was supported with 5 wt% in the same manner. This is designated as 'ZrO_2-bulk MFI 30'.

Fig. 1 shows a comparison of the physicochemical properties of both prepared zeolites. The highly mesoporous ZrO_2[Al]MFI-NS 30 exhibited mesoporous channels which are bound by thin crystalline [Al]MFI walls and which allow the homogenous dispersion of ZrO_2 clusters (bright spots, Fig. 1b). The comparable diffraction intensities are exhibited by XRD, ruling out the collapse of the zeolite framework up on modification with ZrO_2-metal and no diffraction peaks corresponding to a bulk ZrO_2 phase or other crystalline impurities could be detected due to the small size of the ZrO_2 (d_{TEM} = 2.0 nm, Fig. S5†) (Fig. 1c), consistent with the STEM observation. The type IV isotherm

readily reflects the hierarchical construct of the ZrO_2-[Al]MFI-NS 30 sample (Fig. 1d). Fig. 1e shows the pore size distribution for the microporous channels with diameters of *ca.* 0.55 nm and the mesoporous channels with diameters of *ca.* 6 nm (Fig. 1e, insert). Unlike ZrO_2-[Al]MFI-NS 30, as shown in the STEM image in Fig. 1a, the deposited ZrO_2 nanoparticles ($d_{TEM} \sim 16$ nm, Fig. S5†) of the bulk-MFI 30 zeolite are composed of relatively large aggregates measuring up to a few hundreds of nanometers and are located on the external surfaces (Fig. 1a). As anticipated, only the microporous structure (0.55 nm) was confirmed as shown in Fig. 1e.

Table 1 shows the total pore volume, micropore volume and the BET surface area and external surface area of the synthesized zeolites. The result indicated that mesoporous MFI-NS showed a higher BET and external surface area compared to the bulk-MFI 30 due to the mesoporous structure. After the deposition of ZrO_2, the pore volumes and surfaces areas of both zeolites were slightly decreased, indicating the ZrO_2 nanoparticles could be adhered into the porous structure.

The deposition of ZrO_2 nanoparticles (LA-rich sites) within the porous channels (BA-rich sites) on the zeolite provides spatial heterogeneity of the acid sites, as required by the reacting molecules when diffusing along the porous channel. However, only a handful of metals, *e.g.*, Pt with sufficiently high atomic binding energy can exist as clusters small enough to be confined within the narrow width of the 10 MR microporous channels (5.1 × 5.5 Å, 5.3 × 5.5 Å) of the MFI topology;[32] thus,
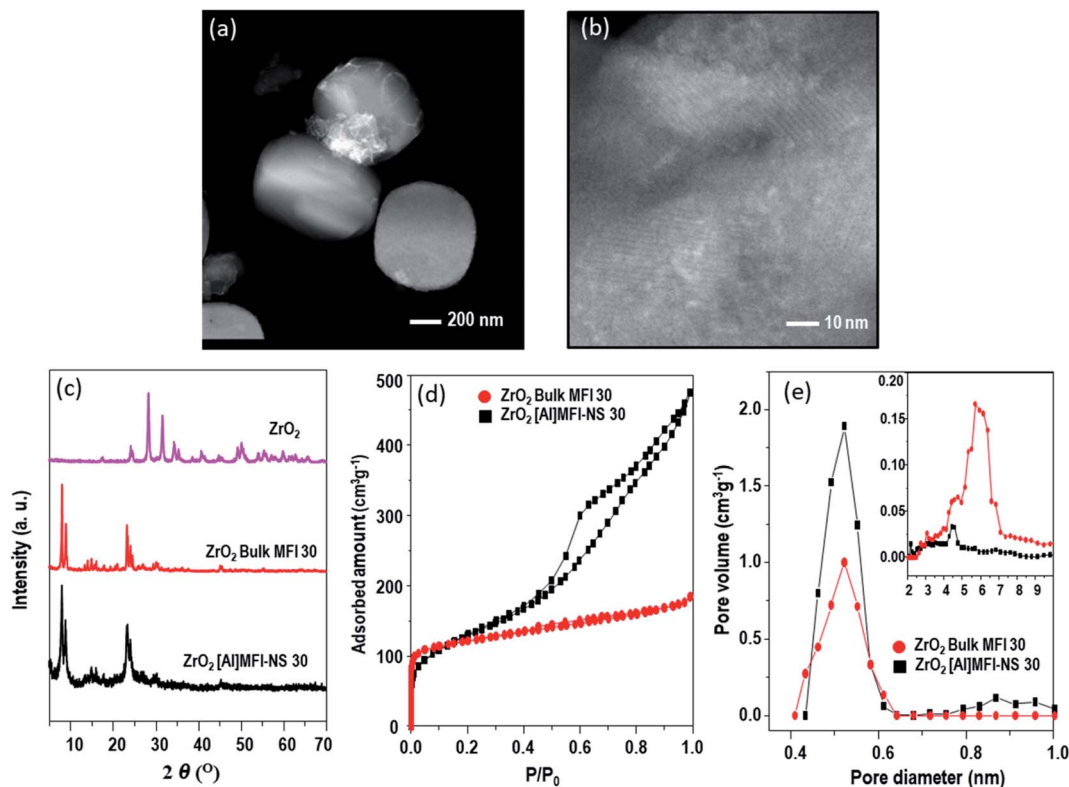

Fig. 1 STEM images of (a) ZrO_2-bulk-MFI 30, (b) ZrO_2-[Al]MFI-NS 30, and the corresponding (c) XRD patterns, (d) Ar adsorption–desorption isotherms, and (e) pore size distributions.

Table 1 Physicochemical properties of the various zeolite catalysts used in the current study

Catalyst	Pore volume (cm³ g⁻¹)		Surface area (m² g⁻¹)	
	$V_{tot}{}^a$	$V_{micro}{}^a$	$S_{BET}{}^b$	$S_{ext}{}^c$
[Si]MFI-NS	0.67	0.09	582	375
[Al]MFI-NS 30	0.69	0.09	577	382
[Al]MFI-NS 60	0.64	0.1	589	365
[Al]MFI-NS 100	0.69	0.1	590	371
Bulk-MFI 30	0.19	0.13	379	81
ZrO₂-[Si]MFI-NS	0.56	0.058	518	346
ZrO₂-[Al]MFI-NS 30	0.59	0.076	510	339
ZrO₂-[Al]MFI-NS 60	0.56	0.086	516	326
ZrO₂-[Al]MFI-NS 100	0.64	0.09	516	310
ZrO₂ bulk-MFI 30	0.14	0.12	339	72

^{a} V_{tot} and V_{micro} are the total pore volume obtained at $P/P_0 = 0.95$. ^{b} S_{BET} is the BET surface area obtained from Ar desorption in relative pressure range (P/P_0) of 0.05–0.20. ^{c} S_{ext} is the external surface area evaluated from the t-plot method.

the ZrO₂ nanoparticles on the zeolite tend to migrate to the external surface area, as mentioned in the Introduction. Because the deposition of ZrO₂ nanoparticles onto the bulk-MFI-30 sample was limited to their exterior surface (72 m² g⁻¹, Table 1), these nanoparticles formed large aggregates of ZrO₂ nanoparticles. In contrast, the ZrO₂-[Al]MFI-NS exhibited

the highly porous nature of a mesoporous material with a high external surface (339 m² g⁻¹, Table 1), which assisted with the dispersion of the ZrO₂ into tiny separated nanoparticles due to a confinement effect between the two adjacent mesopore walls, preventing the further agglomeration of ZrO₂ into large particles.[22,24]

3.2 Acidic properties of the prepared catalysts

The aforementioned investigations have shown the dispersion of the ZrO₂ nanoparticles on the [Al]MFI-NS and bulk-MFI 30 samples, influencing their BA- and LA-properties. Thus, the distributions of BA and LA sites were investigated by FTIR spectroscopy of the adsorbed pyridine.[33] The characteristic vibration of coordinately bonded pyridine at LA (1450–1455 cm⁻¹) was observed. The band at 1555–1560 cm⁻¹ is assigned to pyridine adsorbed at BA, while that at 1490 cm⁻¹ results from for pyridine adsorbed at either BA and LA sites.

As shown in Fig. 2b and c, the deposition of ZrO₂ nano-particles onto ZrO₂-[Al]MFI-NS 30 and 100 samples significantly increased the LA content (from 0.095 to 0.222 mmol g⁻¹ and 0.021 to 0.102 mmol g⁻¹, respectively), as reflected by the increased pyridine-FTIR absorption band centered at 1453 cm⁻¹. Although a significant amount of LA pre-existed as it originated from the octahedral-coordinated framework Al species, as confirmed by ^{27}Al MAS NMR (Fig. S6†), the amount of LA was increased by more than a factor of 3 upon the
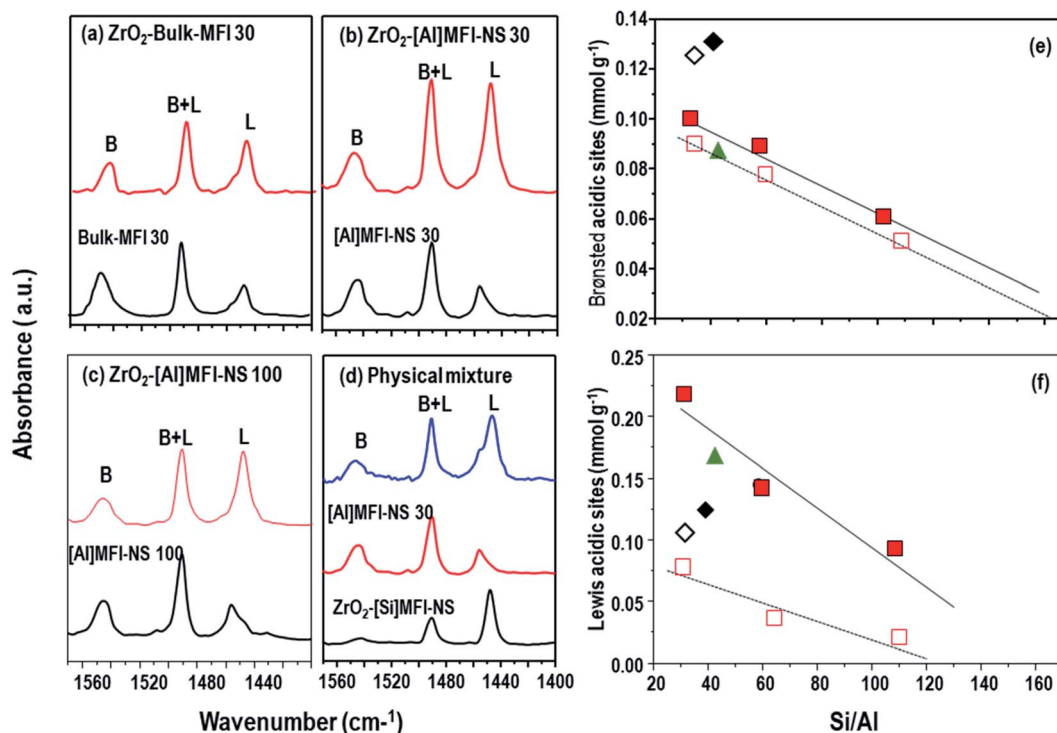

Fig. 2 Pyridine-FTIR spectra of (a) ZrO₂-bulk-MFI 30, (b) ZrO₂-bulk-MFI-NS 30, and (c) ZrO₂-bulk-MFI-NS 100 before and after deposition with ZrO₂, as well as (d) the physical mixture of ZrO₂-[Si]MFI-NS and [Al]MFI-NS 30 and its individual constituents. The quantified density levels of (a) BA and (b) LA sites for the different catalysts before (open symbols) and after ZrO₂ deposition (solid symbols) are also shown. The symbols are as follows: MFI-NS (square), bulk MFI (diamond), and the physical mixture (triangle). The linear lines connecting the data from the MFI-NS samples serve as a guide for the eyes.

deposition of ZrO_2 nanoparticles. This is accompanied by a slight increase in the BA content (1543 cm^{-1}) (from 0.078 to 0.102 mmol g^{-1}, 0.052 to 0.06 mmol g^{-1}, respectively) (Fig. 2b and c and Table 2). This effect can be traced to the partial hydrolysis of the Zr–O–Si bridge to form $Zr(OSi)_3OH$, which has both LA and weak BA properties, as well as that of the surface Zr–OH.[34] By tuning the Si/Al ratio of the [Al]MFI-NS, we further demonstrate the effect on the distribution of the acid sites. As shown in Fig. 2e and f, the amounts and surface density levels of BA and LA can be systematically reduced by up to half when increasing the Si/Al ratio from 30 to 60 and to 100. The description of the BA distribution in ZrO_2 MFI-NS zeolites is completed by considering the external surface acidity (mesoporous MFI wall) with BA density levels of 0.067, 0.057, and 0.036 mmol g^{-1}, as well as the corresponding levels of 0.035, 0.034, and 0.024 mmol g^{-1} of the internal surface area (microporous MFI wall) according to the Si/Al ratio (Fig. S7† and Table 2). The nearly doubled acid content on the mesoporous surface compared to the microporous wall is commensurate with the corresponding measured surface areas. This provides important insight in that the mesoporous channels not only enhance the diffusion of the molecules but the immediate mesoporous surface actually exposes more acid sites than the microporous channels.

In the absence of mesoporosity, as in the ZrO_2-bulk-MFI 30 case here, the resultant aggregated ZrO_2 nanoparticles demonstrated a lower increase in the LA content (0.119 mmol g^{-1}) (Fig. 2b and f) in spite of the similar Al/Zr atom ratio compared to the ZrO_2-[Al]MFI-NS (Table 2). Nevertheless, the rich BA sites within the framework of the bulk MFI were unperturbed, explaining the highest BA amount among all samples assessed (0.132 mmol g^{-1}) (Fig. 2a and Table 2). The level of nearly two orders of magnitude of LA sites on the ZrO_2-MFI-NS zeolites compared to the ZrO_2 bulk MFI 30 is attributed to the small ZrO_2 particle size and the greater dispersion on the mesoporous. This indicates that the mesoporous structure provides strong stability of ZrO_2 nanoparticles of a very small size and prevents the surface segregation of ZrO_2, giving rise to an

increased number of LA sites despite the similar Al/Zr atom ratios (Table 2). While the resultant surface-segregated ZrO_2-bulk MFI 30 catalyst contains both BA and LA sites, it is perhaps more suited to short (e.g., two or three steps) cascade reactions, where the reactants would react with the LA prior to entering and/or upon exiting the BA-rich zeolite micropores. Moreover, as will be shown the later, the overall reaction kinetics can be limited by the sluggish diffusion through the bulk MFI crystals.

We carried out additional acidity investigations using physically mixed samples containing ZrO_2-[Si]MFI-NS (as mesoporous LA-rich zeolite) and [Al]MFI-NS 30 (as mesoporous BA-rich zeolite) (Fig. 2e). While both acidity levels of the catalysts compensated for the lack of acidity of these samples, they showed lower acidity levels in both cases compared to the counterpart catalyst (ZrO_2-MFI-NS 30).

3.3 Catalytic properties

3.3.1 Preliminary investigation of the catalytic performance. To showcase the efficacy of the hierarchical BA–LA zeolite catalysts, they were assessed for the one-pot cascade conversion of furfural to GVL in an isopropanol solvent. Isopropanol, besides serving as the reaction medium, also functions as a sacrificial hydrogen donor for the catalytic transfer hydrogenation via the Meerwein–Ponndorf–Verley (MPV) reduction.[35,36] We confirm that with limited LA sites, i.e., [Al]MFI-NS without ZrO_2 deposition, furfural conversion was limited to less than 50%, with a GVL yield of less than 4%, most likely attributed to the inherent LA sites from the octahedral-coordinated Al according to ^{27}Al MAS NMR (Table 3). Likewise, for the [Si]MFI-NS, which lacks both BA and LA, furfural conversion was limited to 2% with a zero yield of GVL (Table 3). While the abundant LA sites of ZrO_2[Si]MFI-NS showed limited overall cascade furfural conversion to GVL, confirming the greater accumulation of FA (65.7%) with a zero GVL yield, the bifunctional ZrO_2[Al]MFI-NS zeolites regained efficient production of GVL (82.8, 81.6, and 78.3%), according to the Si/Al ratio (Table 3), via the cascade conversion of furfural to GVL as will be shown in the next Section. We confirmed that scaling-up

Table 2 Compositions (in Si/Al and Si/Zr atomic ratios), and density levels of LA and BA sites as well as the ratio of BA-to-LA as determined by pyridine-FTIR

Zeolite	Si/Al[a]	Si/Zr[a]	LA$_{tot}$[b] (mmol g^{-1})	BA$_{tot}$[b] (mmol g^{-1})	BA$_{ext}$[c] (mmol g^{-1})	BA$_{int}$[d] (mmol g^{-1})
ZrO_2-[Si]MFI-NS	n.d.[d]	16.8	0.037	0.006	n.d.[d]	n.d.[d]
ZrO_2-[Al]MFI-NS 30	31	15.8	0.222	0.102	0.067	0.035
ZrO_2-[Al]MFI-NS 60	58.6	16.2	0.15	0.091	0.057	0.034
ZrO_2-[Al]MFI-NS 100	101	15.1	0.102	0.06	0.036	0.024
ZrO_2-[Si]MFI-NS + [Al]MFI-NS 30	36	16.8	0.163	0.09	n.d.[e]	n.d.[e]
ZrO_2^ebulk^{e}MFI 30	47.6	16.6	0.03	0.132	0.028	0.104
[Si]MFI-NS	n.d.[d]	n.d.[e]	n.d.[e]	n.d.[e]	n.d.[e]	n.d.[e]
[Al]^{e}FI-N^e 30	32	n.d.[e]	0.078	0.095	0.063	0.032
[Al]MFI-NS 60	61	n.d.[e]	0.031	0.082	0.051	0.031
[Al]MFI-NS 100	110	n.d.[e]	0.021	0.052	0.033	0.019
Bulk MFI	32	n.d.[e]	0.086	0.126	0.027	0.099

[a] Si/metal molar ratio determined by ICP-AES analysis. [b] The number of LAS and BA sites were determined by FT-IR with pyridine adsorption. [c] The number of external BA sites were determined by FT-IR with DTBP. [d] The number of internal BA sites were calculated by BA$_{tot}$ − BA$_{ext}$. [e] Not detected.

Table 3 Furfural conversion and product yields of the different catalysts[a]

Catalyst	Furfural conversion (%)	Product yield[b] (mol%)				
		GVL	FA	AL	IPL	FDA
ZrO$_2$-[Si]MFI-NS	100	0	65.7	27.2	0	7.2
ZrO$_2$-[Al]MFI-NS 30	100	82.8	0	0	17.2	0
ZrO$_2$-[Al]MFI-NS 60	100	81.6	0	0	18.4	0
ZrO$_2$-[Al]MFI-NS 100	100	78.3	0	0	21.7	0
ZrO$_2$-[Si]MFI-NS + [Al]MFI-NS 30	68	45.1	0	6.8	10.7	5.7
ZrO$_2$-bulk-MFI 30	48	0	0.5	26.4	0	21.5
[Si]MFI-NS	2	0	1.5	0	0	0.5
[Al]MFI-NS 30	41	3.4	0.1	13.7	9.2	14.7
[Al]MFI-NS 60	49	3.2	0.2	20.7	9.6	14.9
[Al]MFI-NS 100	39	1.2	0.2	15.2	11.6	10.6

[a] Reaction condition: 170 °C, 36 h; 0.04 M furfural in a 1 : 50 molar ratio of furfural to 2-propanol solution (2-propanol as solvent and hydrogen donor), the mass ratio of the catalyst to furfural was 1 : 2.5. [b] γ-Valerolactone (GVL); furfural alcohol (FA); β-angelica lactone (AL); 2-propyl levulinate (IPL); furfural diisopropyl acetal (FDA).

of the reaction by a factor of 20 (100 ml reaction, 1 g catalyst) yield similar conversion and selectivity as that carried out at the current out at the current small scale (Table S1†).

3.3.2 Cascade conversion of furfural to GVL and kinetic modelling. On the basis of our own experimental observations and previous studies,[36] the suggested catalytic cycles for each step for the one-pot conversion of furfural to GVL is described in Scheme 1 where furfural diisopropyl acetal (FDA) was detected here for the first time, existing in equilibrium with furfural ($K = k_1/k_2$). FDA was synthesized from furfural via acetalization via two 2-propanol molecules. As reported previously,[37–40] the acetalization is normally carried out with strong Brønsted mineral acids (e.g. HCl or H$_2$SO$_4$) or solid Brønsted acids (e.g., Amberlyst 70 or Nafion-H). We verified the observation using Nafion-H, which is a phase-pure BA, showing the exclusive production of FDA (Table S2†).The conversion of furfural to furfural alcohol (FA) (k_3) by MPV reduction involves a six-membered transition state on the catalyst surface, where the 2-propanol and furfural are coordinated to the same LA-catalyzed Zr center.[18] The FA is subsequently etherified to furfural alcohol ether (FE). From here, FE can undergo two pathways: (1) it can be converted to angelica lactone (AL) (k_5) by the addition of water and followed by ring-opening transesterification with 2-propanol to produce the isopropyl levulinate (IPL) (k_6), or (2) it can be directly formed to the IPL (k_4) via the hydrolytic cleavage of the furan ring opening of FE.[41] As a final step in the cascade reactions, the IPL is reduced to GVL (k_7) via the LA-catalyzed MPV reaction.[35,41–43] Strictly speaking, the latter step involves the hydrogenation of IPL to isopropyl 4-hydroxypentanoate (4-HP), which rapidly undergoes lactonization to form GVL. However, due to the rapid lactonization step, 4-HP was rarely detected[41,42,44] and for simplicity, the conversion of IPL to GVL is represented here as a single step. As can be seen above, the cascade mechanism requires different profiles of acid sites at every step, rendering it an ideal test reaction for the engineering of BA–LA zeolite catalysts.

Fig. 3 reveals the kinetics of the furfural conversion and product formation (left) and the pseudo-first-order rate

constants (k_i) (right) based on the cascade mechanism described in Scheme 1. As shown in Fig. 3d–f, all of the mesoporous ZrO$_2$-[Al]MFI-NSs recorded complete conversions within 1 h, attributed to the simultaneous production of FA and FDA. Although both intermediates were the primary reaction products, the former was instantly converted to a subsequent intermediate, i.e., AL or IPL, while the latter reached a maximum concentration before the concentration gradually decreased with time upon the reversible reaction to furfural. With the abundance of LA sites in the mesoporous ZrO$_2$-MFI-NS zeolites, FDA showed a more rapid decrease compared to the other zeolites, attributed to the rapid furfural conversion to FA via the first MPV reduction. This is accordance with the constant rates of FDA to Furfural (k_2) in ZrO$_2$-MFI-NS zeolites (k_2 = 0.03, 0.06 and 0.1 h^{-1} for ZrO$_2$-[Al]MFI-NS at 30, 60 and 100, respectively) compared to ZrO$_2$-bulk-MFI (k_2 = 1.2 h^{-1}). Moreover, the rate constants of the furfural conversion to FA were increased by two orders of magnitude (k_3 = 2.9, 2.0 and 1.8 h^{-1} for ZrO$_2$-[Al]MFI-NS 30, 60 and 100, respectively) compared to the limited LA-sites in the micropore ZrO$_2$-bulk-MFI (k_3 = 0.02 h^{-1}). This finding arose due to the limited number LA-rich sites as a result of the poorly dispersed ZrO$_2$ nanoparticles in the ZrO$_2$-Bulk-MFI 30 sample. The produced FA can be converted to IPL via two different pathways. FA can be converted to AL by the elimination of 2-propanol followed by an addtion of water to the IPL, or via the direct transformation of the IPL via the hydrolytic cleavage of the furan ring opening in FA.[41] Interestingly, the constant rate of FA to AL (k_4) appears to be the overwhelming pathway compared to that of FA to IPL (k_5) over all samples, which was previously found to be correlated with the hydrophilicity and high BA density of the zeolite.[41,45] While reported bifunctional zeolites have showed that FA conversion to IPL was the a rate-limiting step for the overall cascade due to the lack of BA sites,[35,42,45] the abundant BA sites as active sites in ZrO$_2$-[Al] MFI-NS zeolites are unassociated with this bottleneck here. As the BA content in the ZrO$_2$-[Al]MFI-NS increases (by decreasing the Si/Al ratio from 100 to 30), the overall kinetics is improved, especially during the acid-catalyzed slow step of AL to IPL (k_6 =
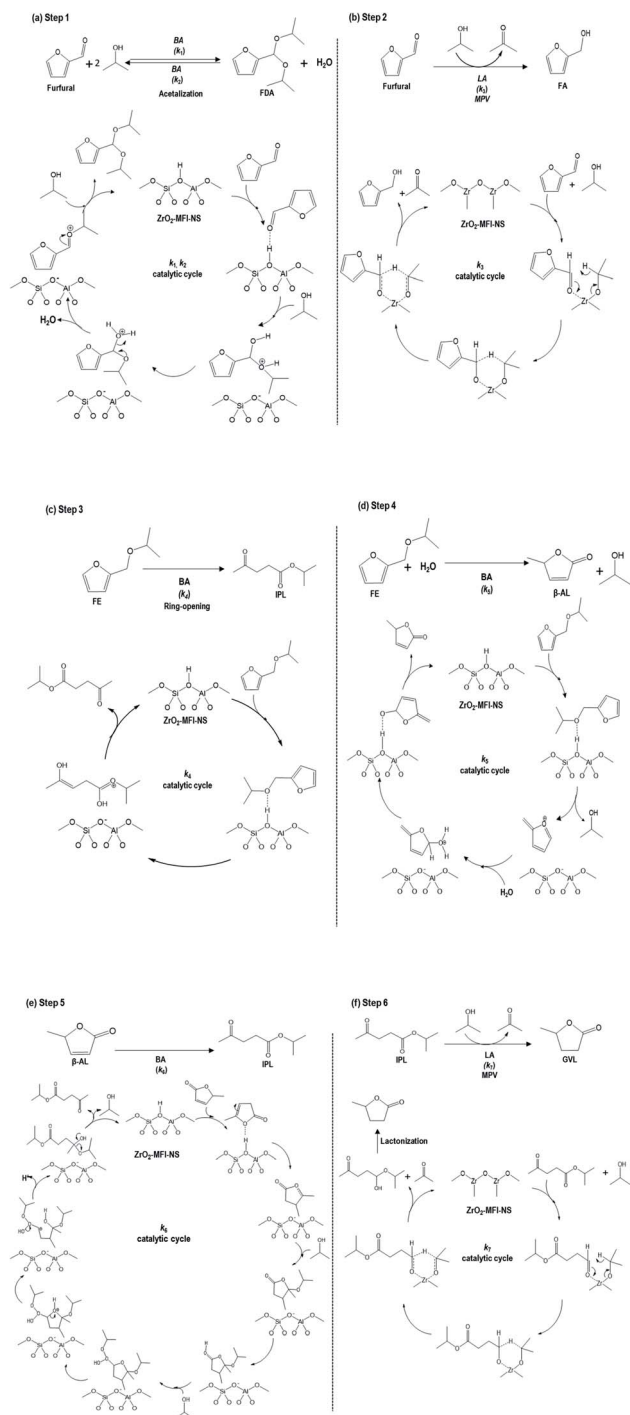
Scheme 1 Proposed catalytic cycles of the cascade reactions for the conversion of furfural to GVL, as adapted from earlier work.[36] (a) Initiation reaction in which furfural was converted into furfural diisopropyl acetal (FDA) (k_1, k_2), (b) furfural to furfural alcohol (FA) (k_3) via MPV reduction, (c) furfural alcohol ether (FE) to the isopropyl levulinate (IPL) (k_4) by direct ring-opening reaction (d) furfural alcohol ether (FE) to angelica lactone (AL) (k_5) by the addition of water, (e) AL to IPL (k_6) by ring-opening transesterification, (f) IPL to GVL (k_7) via the LA-catalyzed MPV reaction (BA: Brønsted acid, LA: Lewis acid).

0.10 to 0.16 h^{-1}, respectively, k_6). The relatively slow hydration kinetics in Step 6 is most likely limited by the non-aqueous solvent used in the current work. A slow step comparable to

that during the conversion of AL to IPL is observed for the final and second MPV reduction of IPL to GVL ($k_7 = 0.12$, 0.11 and 0.08 h^{-1} for ZrO$_2$-[Al]MFI-NS 30, 60 and 100, respectively). While Step 6 is the slow step among the MFI-catalyzed cascades (BA sites), Step 7 is the slow-step on the LA-rich ZrO$_2$ surface. In cascade reactions where there could be multiple active sites catalyzing each of the sequential reaction steps, here we identified two slow steps that require the optimization of the acid distributions on both the MFI framework and the ZrO$_2$ to obtain a high GVL production rate.

As shown Fig. 3a, despite recording a furfural conversion rate of less than 50%, the microporous ZrO$_2$-bulk-MFI produces predominantly of FDA and AL with a trace amount of FA. Again, the slow furfural conversion is related to the limited number of LA-rich sites as a result of the poorly dispersed ZrO$_2$ nanoparticles. While the produced FA is quickly converted to AL, the slow diffusion within the micropores of the bulk MFI crystal for the subsequent conversion to IPL also contributes to the overall sluggish reaction. Possibly in an inter-related fashion, the catalyst only managed a single-pass reaction through the surface-segregated bifunctional catalyst, *i.e.*, Step 3 on the LA sites on the catalyst surface, followed by Step 4 on the BA sites through the bulk zeolite. To exemplify the superiority of BA–LA within a single hierarchical zeolite particle, we carried out another reaction using a physically mixed sample containing ZrO$_2$-[Si]MFI-NS (as a mesoporous LA-rich zeolite) and [Al]MFI-NS 30 (as a mesoporous BA-rich zeolite). As shown in Fig. 3b, a sluggish reaction was found resulting in a furfural conversion of 68%. The low furfural conversion rate is related to the sluggish interparticle diffusion of FDA from the BA-rich zeolite to the LA-rich zeolite. The lower k_3 by more than five-fold compare to that of ZrO$_2$-[Al]MFI-NS 30 resulted in low furfural conversion, an outcome related to the sluggish interparticle diffusion of FDA. Up to this juncture, it is sufficient to say that the careful tuning of the BA–LA sites enhanced the cascade reactions within a single catalyst particle, while the high dispersion of ZrO$_2$ nanoparticles in the mesoporous channels mitigates the overall slow molecular diffusion through the zeolites as well.

On the other hand, bifunctional Zr-Al-beta is known in the literature as a catalyst showing among the best performance capabilities for the conversion of furfural to GVL when Zr-species are introduced after a partial dealumination process.[36,45–47] This sample is denoted as 'ZrO$_2$-Al-beta' (Fig. S4†). We investigated its catalytic performance for the conversion of furfural to GVL as well. A GVL yield of 74.8% was recorded when using the ZrO$_2$-Al-beta catalyst (Fig. S8† (left)). With both the microporous (primary) and macroporous (secondary) dimensions of the ZrO$_2$-Al-beta catalyst (Fig. S4d and e†) larger than those of the ZrO$_2$-[Al]MFI-NS catalysts, diffusion limitation is not expected to be an issue. Rather, the lower GVL yield in the former case is commensurate with the sluggish rate-limiting MPV reduction of IPL to GVL ($k_7 = 0.06$ h^{-1}) (Fig. S8† (right)). This is true despite the relatively efficient conversion of AL to IPL ($k_6 = 0.3$ h^{-1}) likely due to the faster diffusion of molecules through the infiltrating porous channels. Importantly, the ZrO$_2$-Al-beta result consolidates the discussion
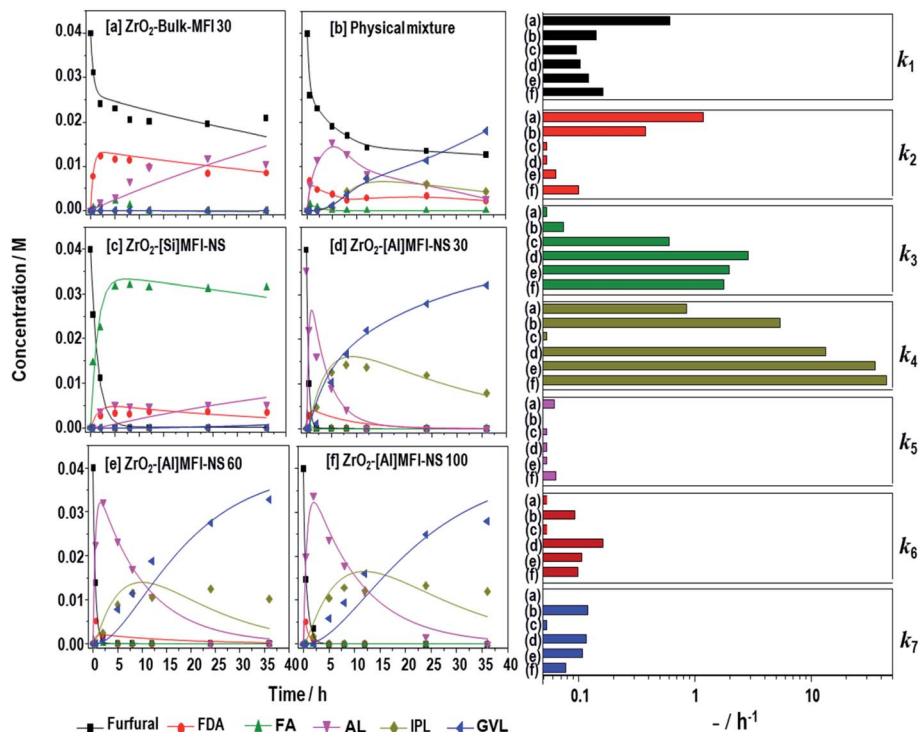
Fig. 3 Kinetic plots of furfural, product GVL and other intermediates over zeolites (left) and the estimated pseudo-first order rate constants based on the mechanism in Scheme 1 (right) for (a) ZrO$_2$-bulk MFI 30, (b) the physical mixture of ZrO$_2$-[Si]MFI NS + [Al]MFI-NS 30, and ZrO$_2$-MFI-NS with Si/Al at ratios of (c) 0, (d) 30, (e) 60, and (f) 100. Reaction condition: 170 °C, 36 h; 0.04 M furfural in a 1 : 50 molar ratio of furfural to 2-propanol solution (2-propanol as the solvent and hydrogen donor), The mass ratio of the catalyst to furfural was 1 : 2.5 under magnetic stirring.
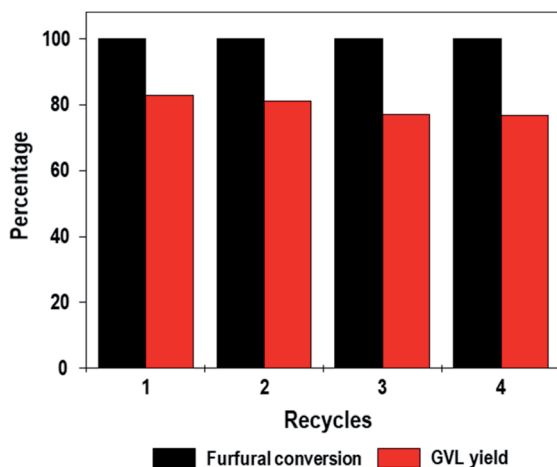

Fig. 4 Recycling experiments of ZrO$_2$[Al]MFI-NS 30 for the one-pot furfural conversion to GVL. Reaction condition: 170 °C, 36 h; 0.04 M furfural at a 1 : 50 molar ratio of furfural to a 2-propanol solution (2-propanol as a solvent and hydrogen donor), The mass ratio of the catalyst to furfural was 1 : 2.5 under magnetic stirring.

above regarding the optimization of both k_6 and k_7 to achieve the highest GVL yield.

3.3.3 Reusability. A reusability test of ZrO$_2$[Al]MFI-NS 30, which is the best performing catalyst for GVL production, was carried out for four times under identical conditions. As shown in Fig. 4, ZrO$_2$ [Al]MFI-NS 30 maintained 100% conversion of

furfural and still higher GVL yields from 76 to 82% during the fourth recycling. The high recyclability of ZrO$_2$[Al]MFI-NS 30 is a result of impressive chemical and thermal stability of the catalyst, as reflected by the well-maintained MFI crystallinity, micro/mesoporous structure, and ZrO$_2$ dispersion, as well as the absence of leaching, even after 4 consecutive reaction runs (Fig. S9†).

4. Conclusion

The work demonstrates the design of mesoporous MFI-NS zeolite catalysts that can be utilized in cascade reactions, as exemplified in the current study in a demonstration of the one-pot conversion of furfural to GVL. The advantage of the highly infiltrated mesoporous channels enabled the deposition of ultrafine ZrO$_2$ nanoparticles (>2 nm) as LA-rich sites throughout the MFI crystal, which otherwise contains predominantly BA and some lesser number of LA sites. These intrinsic MFI acid sites are accessible on the internal surface of the mesoporous channels, as well as the microporous channels contained within the few-unit-cell-thin MFI wall. Besides enhancing the molecular diffusion, the mesoporous channels are an important source of acid sites given that they contain twice as many acid sites as the short microporous channels within the thin MFI. The heterogeneous distribution of LA-rich sites (from ZrO$_2$) and that of mixed BA–LA sites (from the MFI framework) influence the occurrence of the different acid sites experienced by the

molecules as the cascade reactions proceed, hence affecting their kinetics and selectivity. The two slow steps are the conversion of AL-to-IPL and that of IPL-to-GVL, requiring the simultaneous optimization of both MFI and ZrO_2, respectively. A high yield of 82.8% GVL was achieved using the optimum ZrO_2-[Al]MFI-NS 30, an outcome higher than that with the benchmark ZrO_2-Al-beta catalyst (74.8%). We envision that the design concept of the hierarchical BA–LA zeolite shown here can be extended to a range of other cascade acid-base types of reactions. In the same manner, innovative design of other well-ordered, hierarchical BA–LA zeolites especially using economical SDA would pave the way for their wider industrial implementations.

Conflicts of interest

There are no conflicts to declare.

Acknowledgements

References

1 G. W. Huber, S. Iborra and A. Corma, Synthesis of transportation fuels from biomass: Chemistry, catalysts, and engineering, *Chem. Rev.*, 2006, **106**(9), 4044–4098.

2 I. T. Horvath, *et al.*, gamma-Valerolactone - a sustainable liquid for energy and carbon-based chemicals, *Green Chem.*, 2008, **10**(2), 238–242.

3 H. Y. Luo, *et al.*, Investigation of the reaction kinetics of isolated Lewis acid sites in Beta zeolites for the Meerwein-Ponndorf-Verley reduction of methyl levulinate to gamma-valerolactone, *J. Catal.*, 2014, **320**, 198–207.

4 K. Yan, *et al.*, Catalytic reactions of gamma-valerolactone: A platform to fuels and value-added chemicals, *Appl. Catal., B*, 2015, **179**, 292–304.

5 D. M. Alonso, *et al.*, Direct conversion of cellulose to levulinic acid and gamma-valerolactone using solid acid catalysts, *Catal. Sci. Technol.*, 2013, **3**(4), 927–931.

6 W. R. H. Wright and R. Palkovits, Development of Heterogeneous Catalysts for the Conversion of Levulinic Acid to gamma-Valerolactone, *ChemSusChem*, 2012, **5**(9), 1657–1667.

7 D. M. Alonso, S. G. Wettstein and J. A. Dumesic, Gamma-valerolactone, a sustainable platform molecule derived from lignocellulosic biomass, *Green Chem.*, 2013, **15**(3), 584–595.

8 A. Corma, M. E. Domine and S. Valencia, Water-resistant solid Lewis acid catalysts: Meerwein-Ponndorf-Verley and Oppenauer reactions catalyzed by tin-beta zeolite, *J. Catal.*, 2003, **215**(2), 294–304.

9 M. Boronat, A. Corma and M. Renz, Mechanism of the Meerwein-Ponndorf-Verley-Oppenauer (MPVO) redox equilibrium on Sn- and Zr-beta zeolite catalysts, *J. Phys. Chem. B*, 2006, **110**(42), 21168–21174.

10 M. Renz, *et al.*, Selective and shape-selective Baeyer-Villiger oxidations of aromatic aldehydes and cyclic ketones with Sn-Beta zeolites and H_2O_2, *Chem.–Eur. J.*, 2002, **8**(20), 4708–4717.

11 B. Tang, *et al.*, Improved Postsynthesis Strategy to Sn-Beta Zeolites as Lewis Acid Catalysts for the Ring-Opening Hydration of Epoxides, *ACS Catal.*, 2014, **4**(8), 2801–2810.

12 P. Li, *et al.*, Postsynthesis and Selective Oxidation Properties of Nanosized Sn-Beta Zeolite, *J. Phys. Chem. C*, 2011, **115**(9), 3663–3670.

13 Z. H. Kang, H. O. Liu and X. F. Zhang, Preparation and Characterization of Sn-beta Zeolites by a Two-Step Postsynthesis Method and Their Catalytic Performance for Baeyer-Villiger Oxidation of Cyclohexanone, *Chin. J. Catal.*, 2012, **33**(5), 898–904.

14 J. Wang, *et al.*, Post-synthesized zirconium-containing Beta zeolite in Meerwein-Ponndorf-Verley reduction: Pros and cons, *Appl. Catal., A*, 2015, **493**, 112–120.

15 J. Dijkmans, *et al.*, Cooperative Catalysis for Multistep Biomass Conversion with Sn/Al Beta Zeolite, *ACS Catal.*, 2015, **5**(2), 928–940.

16 B. Tang, *et al.*, Mesoporous Zr-Beta zeolites prepared by a post-synthetic strategy as a robust Lewis acid catalyst for the ring-opening aminolysis of epoxides, *Green Chem.*, 2015, **17**(3), 1744–1755.

17 M. Shamzhy, *et al.*, New trends in tailoring active sites in zeolite-based catalysts, *Chem. Soc. Rev.*, 2019, **48**(4), 1095–1149.

18 B. S. Rao, *et al.*, One pot selective conversion of furfural to gamma-valerolactone over zirconia containing heteropoly tungstate supported on beta-zeolite catalyst, *Mol. Catal.*, 2019, **466**, 52–59.

19 Y. F. Lin, *et al.*, The synthesis of Lewis acid ZrO_2 nanoparticles and their applications in phospholipid adsorption from Jatropha oil used for biofuel, *J. Colloid Interface Sci.*, 2012, **368**, 660–662.

20 V. V. Kovalenko, *et al.*, Surface chemistry of nanocrystalline SnO_2: Effect of thermal treatment and additives, *Sens. Actuators, B*, 2007, **126**(1), 52–55.

21 Y. Harima, *et al.*, Lewis-Acid Sites of TiO2 Surface for Adsorption of Organic Dye Having Pyridyl Group as Anchoring Unit, *J. Phys. Chem. C*, 2013, **117**(32), 16364–16370.

22 J. Kim, *et al.*, Supporting Nickel To Replace Platinum on Zeolite Nanosponges for Catalytic Hydroisomerization of n-Dodecane, *ACS Catal.*, 2018, **8**(11), 10545–10554.

23 J. C. Kim, *et al.*, Mesoporous MFI Zeolite Nanosponge Supporting Cobalt Nanoparticles as a Fischer-Tropsch Catalyst with High Yield of Branched Hydrocarbons in the Gasoline Range, *ACS Catal.*, 2014, **4**(11), 3919–3927.

24 J. Han, *et al.*, Confinement of Supported Metal Catalysts at High Loading in the Mesopore Network of Hierarchical Zeolites, with Access via the Microporous Windows, *ACS Catal.*, 2018, **8**(2), 876–879.

25 C. Jo, *et al.*, MFI zeolite nanosponges possessing uniform mesopores generated by bulk crystal seeding in the

hierarchical surfactant-directed synthesis, *Chem. Commun.*, 2014, **50**(32), 4175–4177.

26 M. Choi, *et al.*, Stable single-unit-cell nanosheets of zeolite MFI as active and long-lived catalysts, *Nature*, 2009, **461**(7265), 246.

27 C. Lee, *et al.*, High utilization of methanol in toluene methylation using MFI zeolite nanosponge catalyst, *Catal. Today*, 2018, **303**, 143–149.

28 Y. Seo, *et al.*, Characterization of the Surface Acidity of MFI Zeolite Nanosheets by P-31 NMR of Adsorbed Phosphine Oxides and Catalytic Cracking of Decalin, *ACS Catal.*, 2013, **3**(4), 713–720.

29 F. Gulec, F. Sher and A. Karaduman, Catalytic performance of Cu- and Zr-modified beta zeolite catalysts in the methylation of 2-methylnaphthalene, *Pet. Sci.*, 2019, **16**(1), 161–172.

30 J. C. Kim, *et al.*, Mesoporous MFI Zeolite Nanosponge as a High-Performance Catalyst in the Pechmann Condensation Reaction, *ACS Catal.*, 2015, **5**(4), 2596–2604.

31 Y. S. Tao, *et al.*, Mesopore-modified zeolites: Preparation, characterization, and applications, *Chem. Rev.*, 2006, **106**(3), 896–910.

32 M. Zhang, *et al.*, Shape Selectivity in Hydroisomerization of Hexadecane over Pt Supported on 10-Ring Zeolites: ZSM-22, ZSM-23, ZSM-35, and ZSM-48, *Ind. Eng. Chem. Res.*, 2016, **55**(21), 6069–6078.

33 R. Buzzoni, *et al.*, Interaction of pyridine with acidic (H-ZSM5, H-beta, H-MORD zeolites) and superacidic (H-Nafion membrane) systems: An IR investigation, *Langmuir*, 1996, **12**(4), 930–940.

34 L. M. Kustov, *et al.*, Investigation of the Acidic Properties of Zro2 Modified by So4(2-) Anions, *J. Catal.*, 1994, **150**(1), 143–149.

35 S. S. Enumula, *et al.*, ZrO2/SBA-15 as an efficient catalyst for the production of gamma-valerolactone from biomass-derived levulinic acid in the vapour phase at atmospheric pressure, *RSC Adv.*, 2016, **6**(24), 20230–20239.

36 J. A. Melero, *et al.*, Rational Optimization of Reaction Conditions for the One-Pot Transformation of Furfural to gamma-Valerolactone over Zr-Al-Beta Zeolite: Toward the Efficient Utilization of Biomass, *Ind. Eng. Chem. Res.*, 2018, **57**(34), 11592–11599.

37 Y. M. Ren and C. Cai, A green procedure for the protection of carbonyl compounds catalyzed by iodine in ionic liquid, *Tetrahedron Lett.*, 2008, **49**(50), 7110–7112.

38 J. K. Augustine, *et al.*, Highly efficient and chemoselective acetalization and thioacetalization of aldehydes catalyzed by propylphosphonic anhydride ((R) T3P) at room temperature, *Tetrahedron Lett.*, 2012, **53**(37), 5030–5033.

39 A. A. Smirnov, S. A. Selishcheva and V. A. Yakovlev, Acetalization Catalysts for Synthesis of Valuable Oxygenated Fuel Additives from Glycerol, *Catalysts*, 2018, **8**(12), 595.

40 J. M. Rubio-Caballero, *et al.*, Acetalization of furfural with zeolites under benign reaction conditions, *Catal. Today*, 2014, **234**, 233–236.

41 H. W. Zhang, *et al.*, A combo Zr-HY and Al-HY zeolite catalysts for the one-pot cascade transformation of biomass-derived furfural to gamma-valerolactone, *J. Catal.*, 2019, **375**, 56–67.

42 S. Song, *et al.*, Meso-Zr-Al-beta zeolite as a robust catalyst for cascade reactions in biomass valorization, *Appl. Catal., B*, 2017, **205**, 393–403.

43 L. Bui, *et al.*, Domino reaction catalyzed by zeolites with Bronsted and Lewis acid sites for the production of gamma-valerolactone from furfural, *Angew. Chem., Int. Ed.*, 2013, **52**(31), 8022–8025.

44 S. H. Zhu, *et al.*, Integrated Conversion of Hemicellulose and Furfural into gamma-Valerolactone over Au/ZrO2 Catalyst Combined with ZSM-5, *ACS Catal.*, 2016, **6**(3), 2035–2042.

45 H. P. Winoto, B. S. Ahn and J. Jae, Production of gamma-valerolactone from furfural by a single-step process using Sn-Al-Beta zeolites: Optimizing the catalyst acid properties and process conditions, *J. Ind. Eng. Chem.*, 2016, **40**, 62–71.

46 M. M. Antunes, *et al.*, One-pot conversion of furfural to useful bio-products in the presence of a Sn,Al-containing zeolite beta catalyst prepared via post-synthesis routes, *J. Catal.*, 2015, **329**, 522–537.

47 T. W. Zhang, *et al.*, One-pot production of gamma-valerolactone from furfural using Zr-graphitic carbon nitride/H-beta composite, *Int. J. Hydrogen Energy*, 2019, **44**(29), 14527–14535.